# Journal of Materials Chemistry A

## Effect of lithium incorporation on tweaking the electrocatalytic behavior of tantalum-based oxides

SCHOLARONE™
Manuscripts

# ARTICLE

## Effect of lithium incorporation on tweaking the electrocatalytic behavior of tantalum-based oxides

Alireza Shirazi-Amin, [a,] Panteha Toloueinia,[a] Yang Wu,[a] Andrew G. Meguerdichian,[a] Peter Kerns,[b] Steven L. Suib[*,a,b,c]

To study the effect of lithium incorporation on the electrochemical properties and catalytic behavior of tantalum-based oxides, a series of mesoporous lithium-contained tantalum oxides was developed adopting an inverse micelle-based sol gel synthesis method. Four various phases of amorphous $Ta_2O_5$, polycrystalline $LiTaO_3$, $Li_{5.04}Ta_{6.16}O_{17.92}$, and $Li_3TaO_4$ were determined for samples synthesized at Li/Ta ratios of 0.5 (LTO-0.5) , 1 (LTO-1) , 2 (LTO-2), and 3 (LTO-3) repectively. The surface analysis revealed that LTO-2 sample is featured with lower amount of lithium atoms at the surface rather than the bulk of the sample. The electrochemical analysis of LTO samples showed that LTO-2 possesses lower charge transfer resistance extracted from impedance spectroscopy that consequently leads to a better electrocatalytic performance. The LTO-2 electrode also showed a low open circuit potential (OCP) combined with a relatively higher electroactive surface area, thus capable of running an electrooxidation reaction at a potential lower than all other LTO samples. The more negative OCP value of LTO-2 electrode in AA solution states a more facile electron transfer between the analyte and electrode compared to other synthesized samples. Mott-Schottky plots of LTO electrodes are charactrerized by positive slopes which indicate n-type semiconductor behavior. The charge carrier density ($5.5 \times 10^{19}$ $cm^{-3}$) in LTO-2 sample is the lowest among all other samples. The charge carrier density is dependent on the amount of applied lithium in the synthesis confirming various lithium diffusion behaviors in LTO samples. The lower carrier concentration in LTO-2 justifies its higher activity in electrooxidation providing less populated lower unoccupied molecular orbital (LUMO) for the accomodation of electrons extracted from the analyte higher occupied molecular orbital (HOMO). Therefore, LTO-2 showed an improved electrocatalytic performance due to lower charge transfer resistance (higher conductivity) offered by lower amount of lithium atom at its surface and higher oxygen vacancies in the bulk.

## Introduction

Tantalum-based oxides are promising materials applied in many electronic applications. Due to their high dielectric permittivities, tantalum-based oxides are extensively used in capacitor devices.(1) These materials also represent superior chemical and thermal stability under harsh conditions such as extreme acidic or alkaline pHs and elevated temperatures.(2,3) Thermal and chemical robustness along with high electrochemical potential can associatively provide one of the three requirements for electrode materials used in an electrolysis cell: An electrode material should possesses electrocatalytic activity, should be stable, and should have good conductivity. However, poor conductivity and high perturbation potential hinder the electrocatalytic activity of tantalum-based oxides. Consequently, many efforts have been devoted to the modification of tantalum-based oxides for the

purpose of applying these semiconductors in various electrocatalytic reactions. These attempts aim to induce point defects that potentially lead to increasing the conductivity and lowering the work function of tantalum oxides. Yun et al. showed the superior electrochemical properties of $Ta_2O_5$, TaO, and $TaO_x$ applied as a cathode in dye-sensitized solar cells.(4) Electrocatalytic properties of a modified tantalum-based oxide was also tested in the oxygen reduction reaction (ORR).(5) Formation of thin layers of an orthorhombic tantalum oxide thin structure possessing oxygen-vacancy defects on tantalum carbides (TaC) and nitrides (TaN) has been recognized as a boosting factor in ORR activities of TaC and TaN.(6) Sata et al. suggested an oxygen deficient tantalum oxide substrate could significantly enhance the hydrogen adsorption/desorption of an electrode in the hydrogen evolution reaction (HER).(7) A lanthanum-doped tantalum oxide could significantly increase the electrocatalytic activity of a platinum electrode toward methanol and ethanol oxidation by improving the chemical stability and oxygen storage capacity of the composite electrode.(8) Ishihara et al. showed oxygen vacancies induced by a distortion in crystalline structure of an orthorhombic tantalum oxide facilitated four-electron oxygen reduction reaction (ORR).(9) Nitrogen doping that simultaneously leads to higher conductivity and oxygen vacancy inclusion in metal oxides, has been reported as an

[a.] Institute of Materials Science, University of Connecticut, Storrs, CT 06269, United States.
[b.] Department of Chemistry, University of Connecticut, Storrs, CT 06269-3060, United States.
[c.] Department of Chemical & Biomolecular Engineering, University of Connecticut, U-3222, 191 Auditorium Road, Storrs, Connecticut, 06269, USA.

alternative strategy for increasing ORR activities of tantalum oxide.(10) Possessing multiple redox couples and high redox potential render tantalum-based oxides as good candidates for anode materials in lithium ion batteries.(11,12) Oxygen-deficient tantalum oxides prepared by cathodic polarization treatment (electrochemical reduction) were reported as promising electrocatalysts applied as cathode materials in proton-exchange membrane fuel cells and the hydrogen evolution reaction (HER).(13,14) Yun et al. explored the platinum-like electrocatalytic behavior of tantalum oxide exploited for $I_3^-$ reduction in dye-sensitized solar cells.(4) In this work, the superior activity of the tantalum oxide non-Pt counter electrode was explained by the low oxygen to metal ratio. Besides the mentioned applications (ORR and HER) for tantalum-based oxides as the cathode material, Xiao et al. discovered an unprecedented activity of an oxygen-rich $Ta_2O_x$ (x>5) in the oxygen evolution reaction (OER).(15) A unique surface structure ((200)-surface-exposed $Ta_2O_{5.25}$ nanolayer) formed by controlling the oxygen environment, was reported as an active site that enabled the OER activity of the previously reported inert $Ta_2O_5$. Xia et al. adopted defect engineering as a strategy to unleash the potential of a nanoporous $Ta_2O_5$ as a lithium battery electrode through incorporation of an oxygen-deficient $Ta_2O_5$ thin layer formed by calcination at elevated temperature in argon flow.(16) From a different research perspective, the capacitance behavior of series of $Ta_2O_5$ produced in various oxygen concentrations was thoroughly studied. The electrochemical characterization of these metal oxides demonstrated that capacitive properties of oxides dominate at higher oxygen levels. This investigation proposed that defect-enriched $Ta_2O_5$ surfaces are more prone to corrosion, which means they are more electrochemically active.(17) Gritsenko et al. studied a nonstoichiometric tantalum oxide ($Ta_2O_x$, x<5) to shed light on the charge transport carriers as well as the nature of electronic traps emerging after the synthesis process. DFT calculations in this study revealed that oxygen vacancies act as traps that facilitate electron hopping throughout the oxide.(18) All the mentioned research from different groups are common in incorporation of oxygen vacancies to activate the chemically inert $Ta_2O_5$. Different strategies were adopted to increase the electronic conductivity of the insulating $Ta_2O_5$ by increasing the oxygen vacancy densities. While these activation methods mostly rely on electrochemical modification, high temperature thermal treatment in an oxygen deficient environment, and sophisticated deposition techniques (e.g. ion beam deposition technique, atomic layer deposition, and etc.), there is a lack of studies of easier (other) methods that may lead to the formation of oxygen vacancies. Moreover, the electrochemical properties of the oxygen-deficient tantalum oxides applied as a biological sensor have not been thoroughly investigated.

Herein, we propose an alternative method for the inclusion of electron traps (oxygen vacancies) by incorporating an alkali metal such as lithium in tantalum-based oxides. Alkali metals have been reported as electronic promoters that can be exploited to modify textural and electronic properties of the surface and bulk of metal oxides.(19–22) Intercalation of electropositive alkali metals enhances the electronic and ionic conductivities of metal oxides by

reducing the average oxidation state of the transition metal and improving ion movement in the crystal lattice, respectively. Other than surface and electronic modification of metal oxides, utilization of alkali metals would lead to an interaction with biological samples through coordination.(23) Lithium-contained tantalum oxides have been reported as functional materials expressing optical and electrical properties. These properties can be manipulated by changing the Li : Ta ratio.(24,25) However, a systematic analysis of electrochemical behavior of lithium-contained tantalum oxides has not been addressed elsewhere. In this work, we thoroughly investigate the electrochemical properties of these oxides, their mechanisms of activation, and active sites in a model electrocatalytic reaction.

## Results

### X-ray Diffraction (XRD)

Crystalline structures of lithium-incorporated tantalum oxides were thoroughly investigated with a Rigaku Ultima IV X-ray diffractometer. Fig. 1 shows phase transitions of synthesized materials as the lithium to tantalum ratio changed from 0.5 to 3.0. At the lowest Li-Ta ratio,
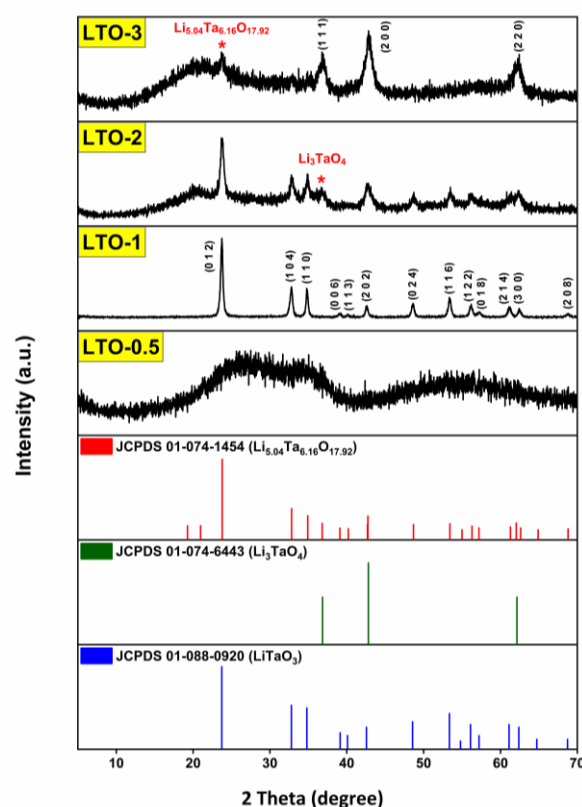


**Fig. 1** XRD patterns of LTO-0.5, LTO-1, LTO-2, and LTO-3 samples (ICDD PDF cards obtained from Rigaku PDXL Software Version 1.8).

XRD showed broad and not well-defined peaks that are characteristic of amorphous structures. According to previous studies of the $Li_2O – Ta_2O_5$ binary phase, a solid solution containing low-temperature amorphous $Ta_2O_5$ and $LiTa_3O_8$ respectively as the major and minor components was proposed as the phase

corresponds to LTO-0.5.(26,27) Increasing the lithium content to an amount where Li:Ta became 1:1 (LTO-1) led to the emergence of a highly crystalline phase which is low-temperature lithium tantalate (L-LiTaO$_3$ - JCPDS No. 01-088-0290) according to the obtained diffraction patterns and Li$_2$O – Ta$_2$O$_5$ phase diagram. Further addition of lithium precursor to the starting sol resulted in the formation of an oxygen deficient lithium tantalate as LTO-2 (Li$_{5.04}$Ta$_{6.16}$O$_{17.92}$ – JCPDS No. 01-074-1454)(28). This phase evolution accompanied by the Bragg diffraction peak broadening accounts for the higher lattice strain and reduced crystallite size. In addition, a diffraction peak at $2\theta = 37^o$ is also observed in the XRD pattern of LTO-2 belongs to the (1 1 1) reflection planes of Li$_3$TaO$_4$. A solid solution phase of Li$_{5.04}$Ta$_{6.16}$O$_{17.92}$ and Li$_3$TaO$_4$ are proposed for LTO-2 that also is consistent with the Li$_2$O-Ta$_2$O$_5$ phase diagram. Further increase of the Li:Ta ratio from 2:1 (LTO-2) to 3:1 (LTO-3) resulted in disappearance of diffraction patterns corresponding to lithium tantalate and emergence of new diffraction peaks. The major reflection peaks ($2\theta = 37^o$, 43$^o$ and 63$^o$) in the XRD patterns of LTO-3 matched with the cubic Li$_3$TaO$_4$ (JCPDS No. 01-074-6443) which was previously reported by Blasse et. al.(29) A broad band seen in the baseline of LTO-3 XRD suggests that an amorphous or low crystalline phase also exists. The small diffraction peak at $2\theta = 24^o$ represents the (0 1 2) planes of L-LiTaO$_3$. The presence of a secondary amorphous phase or semi-crystalline L-LiTaO$_3$ along with Li$_3$TaO$_4$ is in agreement with the Li$_2$O-Ta$_2$O$_5$ phase diagram proposed by Santoro et.al(28).

## Transmission Electron Microscopy (TEM)

To further study the crystalline structure and phase compositions of the synthesized lithium-incorporated tantalum oxides, we used a 300 keV Titan Themis transmission electron microscope (TEM). Fig. 2 illustrates the HR-TEM images of LTO-0.5, LTO-1, LTO-2, and LTO-3 samples along with their lattice fringe measurements. As expected, based on the obtained XRD results, the HR-TEM image showed a non-crystalline porous nature for LTO-0.5. The electron diffraction of this sample depicted hollow rings characteristic of amorphous materials (image inset). At low magnification, the TEM image (Fig. S1 a) of the LTO-1 sample shows a porous nature while in Fig. 2b the HR-TEM image of this material illustrated (0 1 2), (1 0 4), and (1 1 0) as major reflection planes that belong to the LiTaO$_3$ phase. Fig. S8 shows nanopores with sizes of 10-15 nm in diameter embedded within the LTO-1 sample. Also, this TEM image reveals a spongy structure with larger pores formed by interconnected LTO-1 nanoparticles. Selected area electron diffraction (SAED) of the same sample revealed ring patterns indicating the polycrystalline nature of the material (see in Fig. S1 **c**) The low resolution TEM image (Fig. S1 b) of the LTO-2 sample resembles the one acquired for LTO-1 in terms of the shape of particles and their porosities. However, larger particles appeared in the TEM image of LTO-2. At higher magnifications LTO-2 represented crystalline grains embedded in an amorphous matrix that most likely belongs to Li$_3$TaO$_4$ (Fig. 2c) .The lattice fringes analysis of the HR-TEM image obtained from the LTO-2 sample
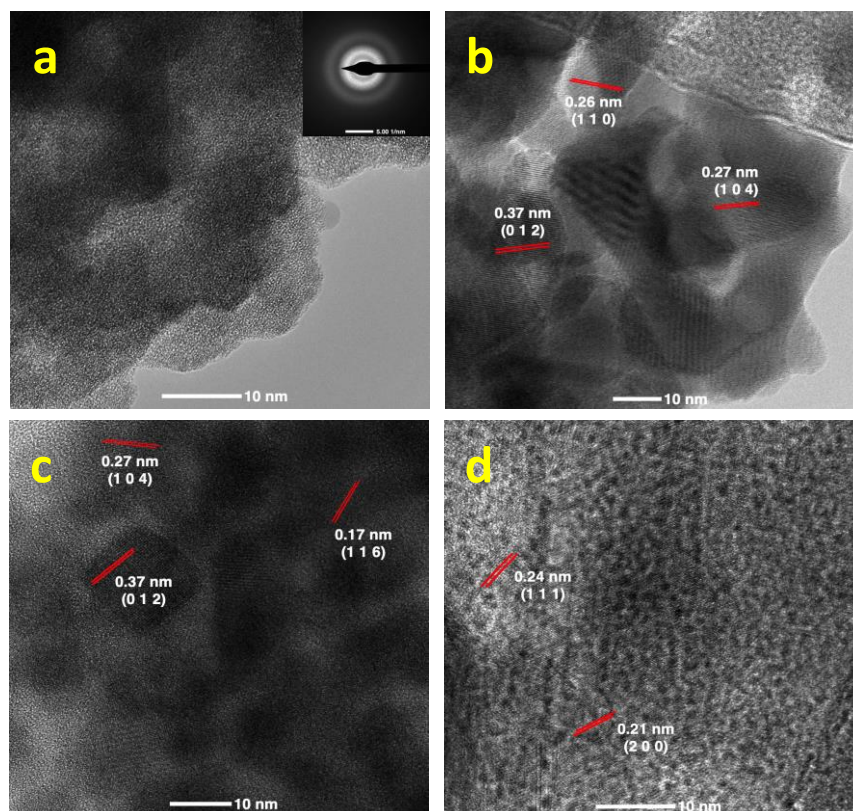


**Fig. 2** HR-TEM images of samples:  a) LTO-0.5. The inset image is the SAED of the captured region that shows hollow rings indicative of an amorphous material.   b) LTO-1 showing reflection planes of (0 1 2), (1 0 4), and (1 1 0) that match with LiTaO3 phase (JCPDS No. 01-088-0290). c) LTO-2 with reflection planes of (0 1 2), (1 0 4), and (1 1 6) corresponds to the oxygen-deficient phase of Li5.04Ta6.16O17.92 (JCPDS No. 01-074-1454). d) LTO-3 showcases cubic Li3TaO8 (JCPDS No. 01-074-6443) with major reflection planes of (1 1 1) and (2 0 0).

showed 0.37 nm, 0.27 nm, and 0.17 nm d-spacing values corresponding to (0 1 2), (1 0 4), and (1 1 6) reflection planes of the $Li_{5.04}Ta_{6.16}O_{17.92}$ phase, respectively. SAED of LTO-1 and LTO-2 samples had similar types of patterns even though these ring patterns in LTO-2 (Fig. S1 d) are comprised of discrete reflection spots which confirmed the presence of coarse grains. HR-TEM images of LTO-3 showed d-spacing values of 0.24 nm and 0.21 nm that belong to (1 1 1) and (2 0 0) diffracting planes in cubic $Li_3TaO_4$.

### Nitrogen Adsorption-Desorption Analysis

The porous nature of the synthesized materials was further analyzed with $N_2$ adsorption-desorption methods. A 6-hour degassing process was done on all samples at 150°C for the duration of 6 hours to remove the entrapped air pockets formed during the synthesis of materials. Brunauer–Emmett–Teller (BET) theory was adopted to determine the surface area of lithium-incorporated tantalum oxides. Barret, Joyner, and Halenda (BJH) methods were exploited to obtain more information about pores diameters, sizes, and their distributions. $N_2$ adsorption-desorption graphs obtained from samples with different lithium contents demonstrated type IV isotherms with a hysteresis loops of type $H_3$ according to the IUPAC classifications.(30,31) The type IV isotherm with a hysteresis loop is an indication of capillary condensation phenomenon that takes place in mesopores .(32) The specific surface areas of different materials were calculated by analyzing the adsorption at the inflection point (relative low pressures) where monolayer adsorption is completed. This analysis showed surface areas of 71, 65, 72, and 82 $m^2/g$ for samples LTO-0.5, LTO-1, LTO-2, and LTO-3, respectively. The emergence of hysteresis loop at different pressure ranges signifies various mesopore/macropore ratios as the lithium content varies (Fig. S2). The hysteresis loop pressure range got narrower as the lithium amount increased in a series of samples. Sample LTO-0.5 showed the widest hysteresis in the pressure range of 0.65-1.00 $P/P_o$, though this pressure range decreased to 0.70-1.00, 0.75-1.00, and 0.78-1.00 for LTO-1, LTO-2, and LTO-3, respectively. This observation determined the lower contribution of mesopores in forming the hysteresis loops for samples LTO-2 and LTO-3 than LTO-0.5 and LTO-1. The type $H_3$ hysteresis loop suggests slit-shape pores for all samples. The further shrinkage and shifting of hysteresis loops to higher relative pressures collectively indicate a decrease of mesoporosity in LTO-2 and LTO-3 samples. Wide pore size distributions of these two samples also support the phase heterogeneity which gives rise to the loss of some portion of mesopores as higher lithium inclusions happen. The other notable feature of the isotherms is the slope of the adsorption branch that represents the strength of the interactions between a sample and a probe molecule ($N_2$ in this case). A strong interaction between a sample and probe molecule leads to a linear slope whereas a weak interaction is associated with a steep slope. As is found from isotherms of samples in this work, the slope of the adsorption branch is successively decreased on increasing the lithium content which is indicative of stronger interactions that occur at higher levels of lithium incorporation.

### Scanning Electron Microscope (SEM)

The microstructures of the synthesized oxides were studied using a FEI scanning electron microscope. The SEM images (Fig. S3) showed the same morphologies for samples synthesized with different amounts of lithium. SEM images revealed the porous microstructures of all samples and they were also studied by TEM and BET analyses. However, the SEM image of LTO-0.5 portrayed smaller particles than three other samples. According to the SEM images and microstructural analysis, increasing the lithium amounts is associated with larger particle formation.

### X-ray Photoelectron Spectroscopy (XPS)

To elucidate the surface species formed following the synthesis of samples with different Li to Ta ratios, XPS was exploited. The survey spectra of LTO samples obtained from the XPS analysis revealed the presence of Ta, O, C and Li on the surface of these samples by showing core states of Ta 4f, Ta 4d, Ta 4p, O 1s, C1s, and Li 1s. High-resolution XPS at binding energies exclusive to each of the observed elements were measured to provide supporting evidence about the nature of atomic layers (~1-10 nm) that comprise the surface of lithium-incorporated tantalum oxides. The emergence of carbon peaks in the XPS survey spectra of LTO samples is attributed to the presence of adventitious carbon which is usually observed in all samples that are exposed to air. Having a known binding energy of 284.8 eV, the adventitious carbon peak is used for the calibration of binding energies of all other elements.  Fig. S4 (a) and (b) display the deconvoluted high-resolution XPS spectra of Ta 4f and O 1s peaks of LTO samples, respectively. High-resolution Ta 4f peaks were deconvoluted using a 30 % Lorentzian/Gaussian (GL (30)) function, a position constraint of 1.9 eV inspired by the 4f $_{7/2}$/4f $_{5/2}$ spin-orbit splitting, and a 4f $_{7/2}$/4f $_{5/2}$ height ratio of 0.75.  The full width at half-maximum (FWHM) used in deconvolution of peaks was done based on work of  Buabthong et al. (33) Fig. S4 (a)  presents deconvoluted Ta 4f peaks for LTO samples consisting of $Ta^{5+}$, $Ta^{4+}$, $Ta^{3+}$ oxidation states representing $Ta_2O_5$, $TaO_2$, and $Ta_2O_3$ at the surface of oxides. While all samples showed all three mentioned oxidation states, the oxidation-state distributions varied significantly for different species. The peaks at 26.04 ± 0.10 eV, 27.04 ± 0.17 eV, and 28.00 ± 0.24 eV are due to $Ta^{3+}$, $Ta^{4+}$, and $Ta^{5+}$, respectively that match with binding energy values reported in the literature for these oxidation states.(34–36)  Observation of lower oxidation states of $Ta^{3+}$ and $Ta^{4+}$, suggests the presence of low-coordinated Ta atoms in the surfaces and sub surfaces of LTO samples. Table 1 summarizes the surface distribution of tantalum oxidation states obtained from the deconvolution of the Ta 4f peak.  According to the tabulated values of the distribution percentages of $Ta^{3+}$, $Ta^{4+}$, and $Ta^{5+}$ oxidation states, LTO-3 has shown the lowest contribution of $Ta^{5+}$ while LTO-2 has revealed the highest percentage of $Ta^{5+}$ on their surfaces. To identify the chemical bonding environments of Li in LTO samples, high-resolution Li spectra were deconvoluted by two Lorentzian/Gaussian fitted curves. The fitted curves exhibited binding energies of 52.7 and 55.9 eV which were attributed to the accommodation of Li atoms at interstitial ($Li_{in}$) and substitutional

(Li$_{Ta}$) sites, respectively. The lower binding energy of Li$_{in}$ determines the lower coordinative interaction of Li atoms with other lattice sites which is characteristic of atoms insertion at interstitial sites(37). The higher binding energy peak located at 55.9 eV is related to the substitutional insertion of Li atoms at Ta sites (Li$_{Ta}$). The binding energy of 55.9 associated with Li$_{Ta}$ matched the Li-O binding energy confirming the substitution of Li at Ta sites(38). The Li 1s spectra of all LTO samples comprised both Li$_{in}$ and Li$_{Ta}$ fitted curves representing binding energies of 52.7 and 55.9 eV. However, calculation of the area under the higher and lower binding energy curves in LTO samples resulted in various contributions of Li$_{in}$ and Li$_{Ta}$ in different samples. According to this analysis, LTO-2 turned out to have the highest contribution of Li$_{in}$ in its Li 1s spectrum (89.8%) while LTO-3 showed the lowest value for  Li atoms inserted at interstitial sites. In general, the following order was obtained for the abundances of Li$_{in}$ in Li 1s spectra of various LTO samples: LTO-2 > LTO-0.5 > LTO-1 > LTO-3. To further investigate the defective nature of LTO samples, high-resolution O1s peaks were also analyzed (See in Fig. S4(b)). O 1s peaks were deconvoluted into three peaks representing crystalline lattice oxygen (O$_{lat}$), oxygen point defects (O$_{vac}$), and adsorbed oxygen species (O$_{ads}$). The peaks in the 530.1-530.3 eV range are attributed to lattice oxygen (O$_{lat}$) while the peaks in ranges of 531.6-531.8 eV and 533.0-533.7 eV represent binding energies corresponding to oxygen vacancies (O$_{vac}$) and adsorbed oxygen species (O$_{ads}$), respectively. The oxygen species distribution percentages represented in Table 1 revealed the following order for the contribution of oxygen vacancies on the first few atomic layers of LTO samples; LTO-3 > LTO-1> LTO-0.5 > LTO-2. The increase in oxygen vacancies in LTO samples was accompanied by the emergence of low-coordinated Ta atoms initiated through a charge compensation process as confirmed by the deconvolution of Ta 4f peaks. Consequently, a nonlinear relationship between the lithium content in LTO samples and oxygen vacancy formation was observed.

**Table 1** Quantification of deconvoluted Ta 4f and O 1s peaks in LTO samples

| Sample | XPS (%) | | | | | |
| --- | --- | --- | --- | --- | --- | --- |
| | Ta$^{3+}$ 4f | Ta$^{4+}$ 4f | Ta$^{5+}$ 4f | O$_{lat}$ | O$_{vac}$ | O$_{ads}$ |
| **LTO-0.5** | 45.07 | 25.60 | 29.33 | 35.72 | 50.57 | 13.71 |
| **LTO-1** | 43.91 | 28.17 | 26.76 | 34.07 | 51.17 | 14.76 |
| **LTO-2** | 37.32 | 27.81 | 34.87 | 48.57 | 42.02 | 9.41 |
| **LTO-3** | 52.82 | 23.62 | 23.51 | 35.59 | 53.63 | 10.79 |

**Q-pole SIMS Analysis**

Quadrupole Secondary Ion Mass Spectroscopy (Q-pole SIMS) was utilized to illustrate the diffusion profile of lithium ion in LTO samples that were Ar$^+$ sputtered over time. Fig. S4 (c) shows the Li ion depth profile analysis of LTO samples. According to the lithium depth profile the following order for the surface lithium concentrations was obtained: LTO-3 > LTO-1 > LTO-0.5 > LTO-2. While the lowest surface concentration (~ 9.00 x 10$^{24}$ atoms/cm$^3$) of lithium ion was observed for LTO-2, Q-pole SIMS revealed that the lithium concentration almost doubled in deeper surfaces of LTO-2 as the Ar$^+$ sputtering time increased. However, lithium depth profiles for all other LTO

samples (LTO-0.5, LTO-1, and LTO-3) show a general decaying trend of lithium atom concentrations. The surface lithium concentration order in LTO samples suggested by Q-pole SIMS shows the same trend as oxygen vacancy order in these samples. This trend similarity implies that the lithium inclusion in the surfaces and subsurfaces of LTO samples is associated with the introduction of oxygen point defects in these atomic layers. The lithium ion concentration decaying trend is observed in all samples except LTO-2 where lithium diffusion to the deeper atomic layers is more feasible.
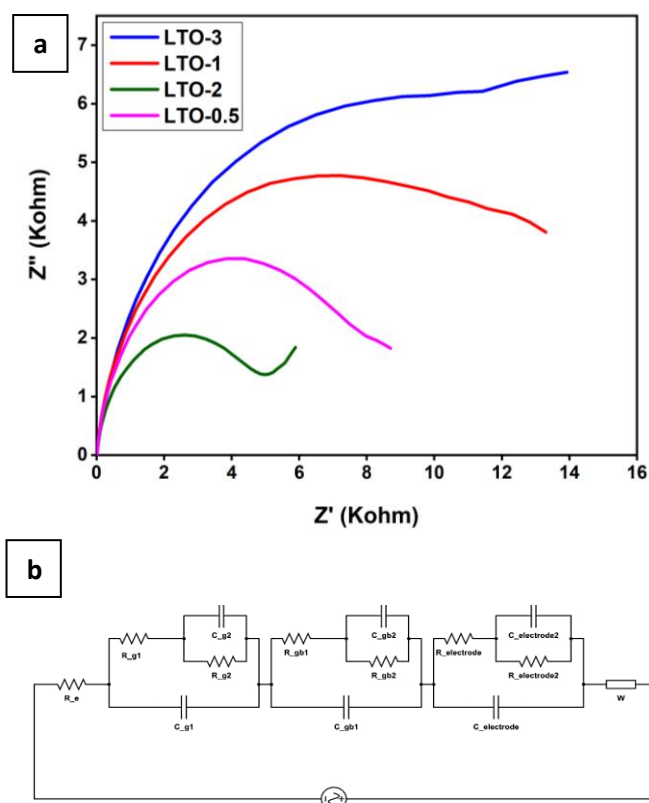
**Electrochemical Impedance Spectroscopy (EIS)**



**Fig. 3** (a) EIS spectra of LTO samples at the frequency range of 1-10$^6$ Hz. (b) Electric equivalent circuit (EEC) obtained from fitting the EIS data of LTO-2.

We adopted EIS methods to investigate the electrochemical performances of a series of electrodes fabricated by drop casting slurries of LTO samples on glassy carbon electrodes. For this purpose, we utilized the Fe (CN)$_6^{4-}$/Fe (CN)$_6^{3-}$ (1:1) redox couple (10 mM) in KNO$_3$ (1 M) solution as an electrochemical probe to study the electron transfer barrier at the electrolyte/electrode interface. We conducted the EIS measurements over the frequency range of 1-10$^6$ Hz at half of the peak potential of the redox event (Fe$^{2+}\leftarrow\rightarrow$Fe$^{3+}$). Fig. 3 (a) shows the Nyquist plots of LTOs. We perturbed the system with an alternating (sinusoidal) potential with an amplitude of 5 mV. The Nyquist plots obtained from impedance studies of all samples possess the same behavior by showing large incomplete semicircles. Representing the charge transfer resistance between the working electrodes and electrolyte, the diameter of the semicircles in Nyquist plots were used to compare the electronic and ionic charge transfer resistances of various LTOs. The semicircle emergence in Nyquist

plots is due to the pseudocapacitive behavior of electrode materials. Such capacitive nature of electrodes increases the charge transfer resistance at the electrode/electrolyte interface. The incomplete semicircles are indicative of the existence of multiple time constants and capacitive components. According to Nyquist plots, the charge transfer resistances observed in LTOs followed the following trend: LTO-3 > LTO-1> LTO-0.5 > LTO-2. LTO-2 showed the lowest charge transfer resistance among all tested materials while LTO-3 was associated with the largest diameter for the semicircle representing the highest value of resistance. Showing the lowest charge transfer resistance, LTO-2 sample has drawn our attention for further study. To establish a better understanding of the electrochemical processes taking place at the surface of the electrode made up of LTO-2 in contact with the solution containing the redox couple ($Fe^{2+}$/ $Fe^{3+}$), we conducted a simulation analysis using an equivalent electrical circuit (EEC) (see Fig. 3 (b)). According to the simulated EEC obtained based on the Nyquist plots for LTO-2, we identified a mixed kinetic and diffusion-controlled mechanism for the redox reaction at the surface of this electrode. The Nyquist plot of LTO-2 electrode confirmed that at high frequencies of AC voltage, current is controlled by the kinetics of the electron transfer between the electrolyte and electrode while at low frequencies mass transfer (diffusion) is dominant. The broad semicircle illustrated by the Nyquist plot suggests the existence of multiple interfaces with superimposed time constants. The presence of three major interfaces in the LTO-2 electrode is proposed based on the simulated EEC. These interfaces formed by grain interior, grain boundary, and electrode/electrolyte effects and each is associated with space charge capacitance ($C$) and polarization resistance ($R$). At high frequency the charge transfer resistance due to the electron and ion movement in grain interior ($R\_g1$) is dominant. However, at medium and low frequencies the charge transfer resistances at the grain boundary ($R\_gb1$) and electrode/electrolyte ($R\_electrode1$) become significant, respectively (39). The capacitive nature of each interface suggested by the existence of space charge capacitance ($C\_g1$, $C\_gb1$, and $C\_electrode1$) in EEC is due to the formation of an electric double layers (EDL). These EDLs form as a result of the adsorption of charged species at each interface. EEC of LTO-2 also suggests the presence of a Warburg impedance ($w$) that manifests a resistance associated with a diffusion-controlled process. This diffusion-controlled process is defined by the redox couple (Fe (CN)$_6$ $^{4-}$/Fe (CN)$_6$ $^{3-}$) mass transfer from the bulk to the surface of LTO-2. The existence of the Warburg impedance confirmed by the 45° straight line in the Nyquist plot of LTO-2 supports the coverage of charged species on the surface of this electrode. The EEC of LTO-2 also suggests the presence of three more interfaces that each comprise both polarization resistance and space charge capacitance. According to EEC the emergence of these interfaces that are located in series with each of the main grain, grain boundary, and electrode/electrolyte interfaces confirms the existence of a secondary phase in LTO-2. This secondary phase is characterized by the occurrence of resistances ($R\_g2$, $R\_gb2$, and $R\_electrode2$) and capacitances ($C\_g2$, $C\_gb2$, and $C\_electrode2$) in EEC corresponding to the grain, grain boundary, and electrode interfaces.

## Potentiodynamic Polarization and Cyclic Voltammetry (CV): Electrocatalytic Oxidation of Ascorbic Acid

Potentiodynamic polarization in tandem with CV can be used respectively as thermodynamic and kinetic tools to help us learn more about the characteristic properties of the electrode materials. For the purpose of collecting more information about EDL formed on lithium-contained tantalum oxides and the adsorption affinity of charged species to these materials the electrodes were polarized. The open circuit potential (OCP) of each electrode was first established by soaking electrodes in AA (5 mmol dm$^{-3}$) solution for one hour. Subsequently, the electrodes were polarized 100 mV in positive and negative directions from their OCPs. According to the obtained polarization curves (see in Fig. S5 a), the LTO-2 sample shows the lowest equilibrium potential between the anodic and cathodic reactions. The equilibrium potentials obtained from polarization curves can be used to qualitatively explain the ease of adsorption of ionic species on electrode materials. The lowest equilibrium potential observed for the LTO-2 sample is indicative of a thermodynamically-more-favorable adsorption of ionic species on the surface of the electrode. The electrocatalytic properties of LTO samples were thoroughly investigated by applying them as the electrode materials in electrochemical oxidation of ascorbic acid (AA) as a small biomolecule. Fig. 4 shows cyclic voltammetry of AA (5 mmol dm$^{-3}$) at various LTO electrodes in a KCl (0.1 mol dm$^{-3}$) solution. Prior to cyclic voltammetry, the AA solution was purged for 15 min to remove dissolved oxygen. During the experiment the surface of the solution was saturated with an inert gas by streaming $N_2$ gas to the top layer of the solution in a way that solution stillness was not perturbed. The potential was swept first in positive direction and then reversed to zero with the scan rate of 20 mVs$^{-1}$. The activities of LTO electrodes in electrooxidation of AA were compared against the performance of platinum, glassy carbon, mesoporous tantalum oxide, and commercial tantalum oxide as materials applied as the working electrode. This comparison study revealed the commercial and synthesized mesoporous tantalum oxides have no or negligible contribution in electrooxidation of AA since non-faradaic processes are detected. This result was also intuitively expected since tantalum oxide is extensively studied as a material with superior dielectric properties. The small non-faradaic current observed for the synthesized mesoporous tantalum oxide is due to the higher capacitance resulting from the porous nature and relatively high surface area of this oxide. These two oxides were studied to rule out the tentative impact of pristine oxides on electrooxidation of AA. This study also adopted glassy carbon and platinum as benchmark

working electrodes in electrochemical oxidation of AA. Among all LTO electrodes, LTO-2 sample showed the best overall activity considering both thermodynamic and kinetic aspects of AA electrooxidation reaction. An anodic peak appeared at E=0.38 V (vs. Ag/AgCl) is attributed to the overpotential required for oxidation of AA at LTO-2 that is lower than the overpotential of AA electrooxidation at a lithium-doped tantalum oxide electrode reported by Wang et al.(2)  The activation overpotential for all LTO samples follows the following trend: LTO-3 > LTO-1 > LTO-0.5 > LTO-2. Activation overpotential consists of two components. One component is the electrical energy resulting from the interaction between ions and the electrode. The other component comes from the activation energy of the charge transfer reaction associated with the analyte oxidation. While the former is controlled by the electrode potential, the latter is governed by the carrier density in the depletion region and charge transfer resistance at the electrode surface. The lowest activation energy obtained at a specific current density (300 µA/cm$^{-2}$) for LTO-2 is due to the relatively lower charge transfer resistance of this electrode as compared to the other LTO samples which was also confirmed by an EIS study discussed previously. Better interaction of the LTO-2 electrode with AA is also established by the lower polarization potential obtained in the potentiodynamic analysis. The charge transfer resistances of all LTO electrodes in AA electrooxidation were also compared to bare glassy carbon and commercial tantalum oxide (Fig. S5 b). Comparison analysis revealed the best charge transfer kinetic was observed for LTO-2 among all LTOs, glassy carbon, and commercial tantalum oxide electrodes.

**Double Layer Capacitance and Electrochemical Surface Area (ECSA)**

To further investigate the contributing factors that lead to different electrocatalytic activities, the electrochemically active surface areas (ECSA) of different tantalum oxides were measured by finding the capacitance of the Helmholtz layer formed on electrodes using cyclic
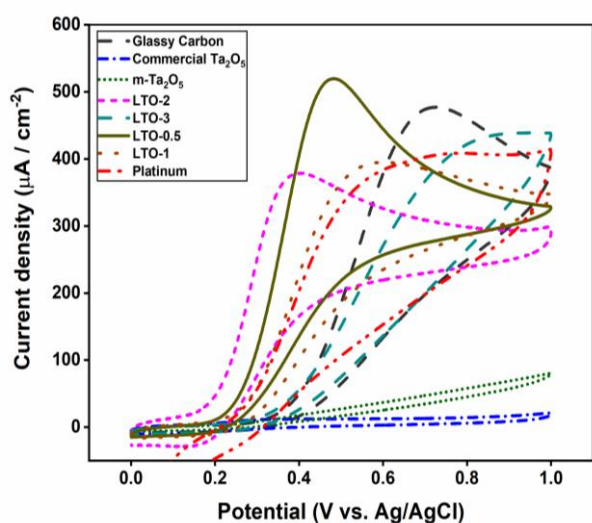


**Fig. 4** Cyclic voltammetry of AA at LTO electrodes.

voltammetry in non-faradaic potential windows of the electrode materials. (40–42) The non-faradaic processes at various LTO

electrodes were studied cycling the electrodes potentials within ±8 mV with respect to their OCPs. Fig. 5 shows voltammograms of LTO electrodes in the solution of AA (5 mmol.dm$^{-3}$) in KCl (0.5 mol.dm$^{-3}$). The "box-like" feature associated with all voltammograms indicates reversible charge and discharge currents characteristic of the capacitive behavior of the Helmholtz layers. To extract the electrochemical double layer (EDL) capacitance of each LTO electrodes, cyclic voltammetry was run at different scan rates (20, 50, 100, 200, 400, and 800 mV). The capacitive charging/discharging currents correspond to the center of the potential window were used to plot the current density (I) versus scan rate (ν). The EDL capacitance related to each of the electrodes was calculated using the following equation.

$$dq/dt = C_{dl}.dv/dt \qquad \text{Eq. 1}$$

The slope of I (dq/dt) vs. ν (dv/dt) plots represents the EDL capacitance. Following the EDL capacitance extraction, the ECSA is obtained from the equation below where Cs stands for the specific capacitance of an ideally flat electrode of 1 cm$^2$ (20-60 µF). The following order was observed for the double layer capacitance of LTO electrodes: LTO-2 (36 µF/cm$^2$) > LTO-0.5 (30 µF/cm$^2$) > LTO-1 (21 µF/cm$^2$)> LTO-3 (23 µF/cm$^2$). EDL studies revealed that the ECSA of LTO-2 electrode is the highest among all synthesized oxides. This
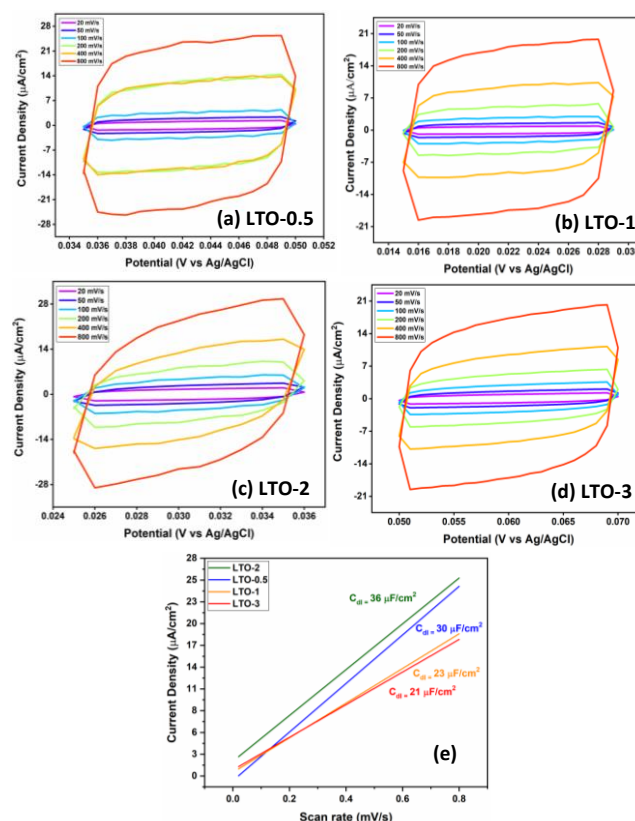


**Fig. 5** Helmholtz layer capacitance measurements for the extraction of electrochemical surface area of LTO electrodes. (a-d) Potentials scanned in non-Faradaic regions of LTO electrodes at scan rates of 20 mVs$^{-1}$, 50 mVs$^{-1}$, 100 mVs$^{-1}$, 200 mVs$^{-1}$, mVs$^{-1}$, and 800 mV/s. (e) I vs. ν plot: slopes of lines are utilized for the comparison of C$_{dl}$ in various LTO electrodes.

higher electrochemical surface area of the LTO-2 electrode, which was also supported by higher geometrical exchange current density at its OCP, confirmed the higher activity of this electrode toward the electrooxidation of ascorbic acid.

**Mott-Schottky Analysis; Carrier Density and Flat Band Measurements**

Total capacitance (C) of a semiconductor/electrolyte interface comprises the Helmholtz capacitance ($C_H$) governed by the electric double layer on the electrolyte side, and space charge capacitance ($C_{SC}$) on the semiconductor side. However, the total capacitance of the semiconductor/electrolyte interface is dominated by the space charge formed on the semiconductor side knowing that the Helmholtz capacitance is a large value as compared to the space charge capacitance and consequently has a small contribution toward the total capacitance according to the following equation(43):

$$1/C = 1/C_H + 1/C_{SC}$$ **Eq. 2**

The total capacitance of the semiconductor/electrolyte interface can be obtained from impedance spectroscopy adopting the following equation(44):

$$C = -1/2\pi f Z_{img}$$ **Eq. 3**

In the above equation, $f$ is the frequency and $Z_{img}$ is the imaginary impedance. The imaginary impedance associated with the semiconductor/electrolyte capacitance system can be obtained from the EIS that is performed at a constant frequency and varied potentials. The chosen frequency for the $Z_{img}$ measurements should be high enough (short time scale) that does not allow the semiconductor/electrolyte interface to be filled and is subsequently unfilled with slow-moving ions present in the electrolyte. Selecting an appropriate frequency is critical to isolate the space charge capacitance from the double layer capacitance. The semiconductor/electrolyte interface can be further explained by Mott-Schottky analysis using the data that are obtained from EIS measurements at a certain frequency and applying them in Eq. 4. The flat band potential and charge carrier density can be determined by Mott-Schottky analysis providing the relationship between the total semiconductor/electrolyte interface capacitance and applied potentials, given by:

$$1/C^2 = (2/e\varepsilon_r\varepsilon_o N_d)(-V+V_{fb}-KT/e)$$ **Eq. 4**

Where $N_d$, V, $V_{fb}$, K, and T are charge carrier concentration, applied potential, flat band potential, Boltzmann's constant, and absolute temperature, respectively. $\varepsilon_r$ and $\varepsilon_o$ are also the dielectric constants of the semiconductor and air(45).
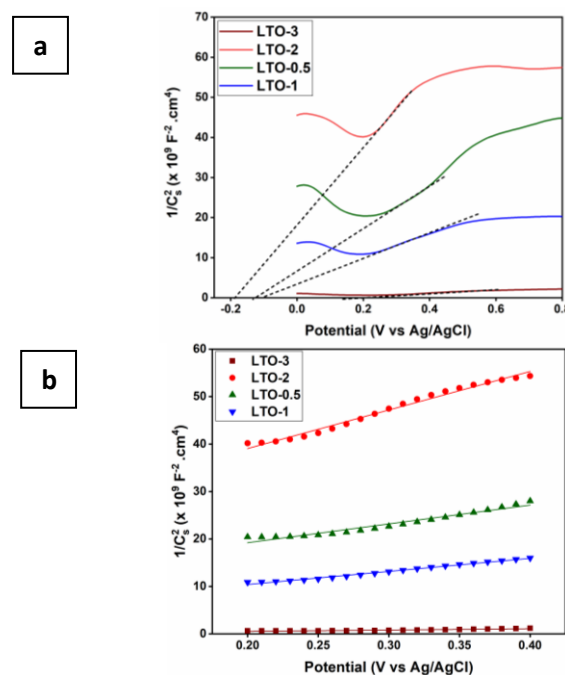


**Fig. 6** (a) Mott-Schottky plots for LTO-0.5, LTO-1, LTO-2, and LTO-3 electrodes.

The Mott-Schottky plots of LTO-0.5, LTO-1, LTO-2, and LTO3 are shown in Fig. 6. All Mott-Schottky plots represent the same type of graphs with a linear positive slope in the potential range from +0.2 to +0.8 V. The positive slope in the Mott-Schottky plots is an indication of n-type semiconductors. The charge carrier (electrons for n-type semiconductors) densities are calculated utilizing the slope of the linear regions of the Mott-Schottky plot and Eq. 5. Mott-Schottky plots show the following order was obtained for the charge carrier density in LTO samples: LTO-3>LTO-1>LTO-0.5>LTO-2. The density of charge donors, that could be a result of oxygen vacancies, defective structures, or interstitial cations, is found to be the lowest value in LTO-2 among all other samples. The flat band potential of semiconductors that can be determined from the *x*-intercept of the linear region in the Mott-Schottky plot is adopted to determine the contact potential between the semiconductor and electrolyte. The value of this potential indicates the feasibility of charge transfer across the semiconductor/electrolyte interface. The flat band potential measurements in LTO samples suggest that LTO-2 has the lowest flat band potential. Less electrical energy is required to transfer an electron from the electrolyte to the LTO-2 sample. As the energy model proposes, in n-type semiconductors when a potential, higher than the flat band potential of the semiconductor is applied, the surface of the semiconductor undergoes electron accumulation. According to the Mott-Schottky analysis of LTO samples, in the linear region of the slopes (0.2-0.8 V), the applied potentials are higher than the flat band potentials in all LTO samples. This means that the surfaces of all LTO samples have entered the electron accumulation mode. LTO-2 is associated with the lowest carrier density that is equivalent to the lowest negative charge accumulation on the surface of this LTO sample. Flat band potentials and carrier concentrations obtained from Mott-Schottky plots of LTO sample are

reported in Table 2.

**Table 2** Carrier densities ($N_d$) and flat band potentials of LTO samples

| Sample | Carrier density, $N_d$ (cm$^{-3}$) | Flat band potential (V) |
|---|---|---|
| LTO-0.5 | $5.5 \times 10^{19}$ | -0.20 |
| LTO-1 | $1.6 \times 10^{20}$ | -0.13 |
| LTO-2 | $1.2 \times 10^{20}$ | -0.10 |
| LTO-3 | $1.2 \times 10^{23}$ | 0.20 |

### Diffusion vs Adsorption of AA on LTO-2 Electrode

Electrooxidation of AA on LTO-2 is scrutinized further for the sake of finding the mechanism and kinetic model that explain the oxidation reaction at the surface of the electrode material. Two models have been frequently used for the description of the adsorption kinetics at the electrode/electrolyte interface. The interparticle diffusion model is used when the rate determining step is the mass transfer of the electrolyte to the electrode surface sites, whereas the adsorption model is proposed to be used when the overall rate of the electrolyte sorption on the electrode is governed by the surface reaction rate.(46) According to the Randles-Sevcik equation, the faradic current density depends on the scan rate. However, other than the faradaic current the charging current also increases with the scan rate. While faradic current is proportional to the square root of the scan rate ($I_F = 0.4463nFAC (nF_vD/RT)^{1/2}$), the charging current linearly changes as the scan rate varies ($I_c = C.\nu$). For the reaction studied in this work, the charging current is due to the adsorption of deprotonated ascorbic acid (AA-) on the surface of the LTO-2 electrode whereas, faradaic current is due to diffusion of AA- species to the electrode surface. Fig. S6 a illustrates the cyclic voltammograms of AA at LTO-2 when the scan rate varies from 5 to 400 mVs$^{-1}$. These voltammograms show that the anodic peak increased as the scan rate. In Fig. S6 b the anodic peak currents were plotted against the scan rate and square root of the scan rate, respectively to understand whether the reaction is controlled by adsorption or diffusion. Linear regression was used to model the relationship between current and scan rates. Having high $R^2$ values, both graphs exhibited a high degree of linearity which indicates the mixed diffusion and adsorption-controlled mechanism of AA oxidation at the LTO-2 electrode. However, the fitted lines in these graphs exhibited various $R^2$ values for different ranges of scan rate. While higher values of $R^2$ at low scan rates for graph A suggest a diffusion-controlled process, an adsorption dominant process is determined by higher values of $R^2$ in graph B. AA oxidation on LTO-2 comprises diffusion and adsorption-controlled processes that take place at different scan rates. The higher overpotential observed for the oxidation of AA at the scan rate of 400 mVs$^{-1}$ is due to the adsorption and accumulation of AA on the surface of LTO-2 followed by a harder diffusion of AA from the bulk of the solution to the electrode surface. While at low scan rates AA has enough time to diffuse through the adsorbed layer and gets oxidized on the surface of LTO-2, at high scan rates mostly surface adsorbed AA gets oxidized and the diffusion is hindered by the adsorbed layer. The presence of this adsorbed layer on the LTO-2 electrode was previously confirmed by EEC obtained from the fitting of the EIS spectrum.

### Oxidation Mechanism of AA on LTO-2: Bulk vs. Surface reactions

The LTO-2 electrode was dipped in the 5 mmol.dm$^{-3}$ AA solution for 5 seconds. The electrode was rinsed with distilled water for a couple of times and CV was run on the electrode between -0.4 and 1.0 V vs Ag/AgCl in a solution of pure supporting electrolyte (KCl 0.1 mol.dm$^{-3}$). CV illustrated a chemically reversible but electrochemically irreversible reaction by showing anodic and cathodic currents separated with a potential larger than 59 mV which is characteristic of an electrochemically reversible reaction. However, the cathodic current was either not observed or negligibly detected when the CV of LTO-2 was run in the solution of AA at a slow scan rate of 20 mV/s (see in Fig. S7). The emergence of redox peaks in the voltammogram of the electrode, that was previously submerged into AA solution for a short period of time (5s), is related to the reaction that occurs on the surface of the electrode. As the ascorbic acid readily dissociates into ascorbate anion (AA-) in an aqueous solution, the presence of redox peaks for a solution where no AA molecule exists in the bulk solution confirms the adsorption of AA- on the surface of the electrode followed by an one-electron oxidation step into ascorbyl radical (AA$^{•-}$). The symmetric voltammogram confirms the 1 e-, 1 H+ reversible oxidation of monoanionic ascorbic acid to ascorbyl radical anions which had been previously proposed by Hu et al.(47) The lower peak current and higher overpotential associated with the anodic peak current in the surface reaction, in comparison to the bulk electrooxidation of AA, which shows that electron transfer can potentially take place through two types of active sites, one at the outermost layer of the catalyst and one at a deeper layer where AA molecule diffusion would dominate. Comparing CVs obtained from bulk and surface reactions, the surface sites need higher electrical energy input to become activated and they are limited to provide the energy of one electron transfer within the applied potential, while the bulk reaction offers a lower overpotential required for 2 e- oxidation of AA.

## Discussion

Alkali metal incorporation into metal oxides has been considered as a method to change the surface and bulk properties of the oxides.(20–22,48–52) The textural and structural feature alterations triggered by alkali metals are attributed to the electronic effects of these metals on metal oxide-based substrates. Consequently, alkali metal compounds are potentially exploited as electronic promoters for metal oxide-based catalysts in different catalytic reactions. The promotion effect of alkali metals may be theoretically explained by changes in various properties of metal oxides such as crystalline structure, specific surface area, charge carrier concentration, and chemical environment or valence state of the transition metal ions.(48) One well-known effect of doping of transition metal oxides with alkali metals, which possess a +1 oxidation state, is the hole

formation in the oxide lattice that is followed by an oxygen atom removal step. Alkali metal dopants are reported to have a preference for promoting the migration of oxygen atoms located at intra layers of the lattice than the oxygen atoms across the transition metal cation layers.(50) These oxygen vacancies are experimentally proven to be really stable that cannot be annealed even in the presence of excess amounts of oxygen.(53,54) A second oxygen species known as "active oxygen" can be removed from the oxide lattice following the oxygen vacancy formation. The active oxygen vacancy is associated with a low activation energy making removable from the distorted lattice more favourable than the first oxygen from the undoped metal oxide. The formation of the active oxygen vacancy determines the reducibility of the alkali metal incorporated metal oxide. The active oxygen vacancies act as electron donors and become positively charged. The formation of ionized oxygen vacancies leads to the liberation of electrons to the oxide lattice. These released electrons can be considered either delocalized in the oxide conduction band or localized at a metal ion on a normal lattice site. If the latter happens the valence state of the transition metal reduces to lower oxidation states and suboxides will form ($MO_{x-1}$). The pure tantalum oxide ($Ta_2O_5$) is known as a non-reducible oxide, possessing no electrons in the d orbitals of Ta ($d^0$). Electron migration between oxygen 2p orbitals (valence band) and tantalum 5d orbitals (conduction band) is not thermodynamically favored unless new energy levels are introduced to the $Ta_2O_5$ band gap. Formation of oxygen deficient tantalum oxides which are synthesized by adopting different methods including pulsed laser deposition (PLD), atomic layer depositions (ALD), chemical vapor deposition (CVD), sputtering, and electrochemical deposition have been previously reported. Lithium as an alkali metal dopant that has fairly similar atomic (0.152 nm) and ionic radii (0.068 nm) to tantalum (0.143 and 0.070 nm), can be exploited to induce oxygen vacancies. Sweeney et al. also reported electrons being trapped in $LiTaO_3$ following oxygen vacancy inclusion processes performed in an argon environment at high temperatures.(55,56) A chemical reduction technique in tandem with annealing at high temperatures in inert medium was also used by Yan et al. to prepare reduced lithium tantalite ($LiTaO_{3-x}$).(57) Creation of oxygen vacancies in tantalum oxide is accompanied by the reduction of tantalum through the introduction of localized electrons at the 5d orbitals of tantalum. Upon the lithium addition to the tantalum-based oxide lattice, the reduction of $Ta^{5+}$ is promoted through crystalline lattice distortion and introduction of electron density to the band gap. These cascade events can theoretically lead to a higher conductivity of the lithium-incorporated tantalum oxide in comparison to the pure parent tantalum oxide. In this work, a series of lithium-incorporated tantalum oxides were synthesized, and their electrochemical properties were scrutinized in order to find a solid structure-reactivity relationship. The EIS study revealed that the LTO-2 electrode is associated with lowest charge transfer resistance among all other samples. According to EEC simulation three interfaces including main grain, grain boundary, and electrode/electrolyte are suggested for LTO-2 sample. Moreover, a secondary phase might be present in this sample as EEC suggests. The XRD analysis also confirms the presence two phases. The major

phase is turned out to be $Li_{5.04}Ta_{6.16}O_{17.92}$ which is accompanied by a trace amount of $Li_3TaO_4$. As $Li_3TaO_4$ is the major phase in LTO-3, the lower charge transfer resistance observed in LTO-2 could not be due to the presence of $Li_3TaO_4$ in LTO-2. HR-TEM and XRD both show the same reflection planes and d-spacing values corresponding to these reflections in LTO-1 and LTO-2. However, LTO-2 is significantly more conductive than LTO-1 according to EIS studies. The SAED discrete spot pattern of LTO-2 indicates a coarse-grained polycrystalline material, while the SAED of LTO-1 represents a continuous pattern which is characteristic of a fine polycrystalline microstructure. Possessing a coarse polycrystalline structure, LTO-2 offers larger grain size and consequently a decreased grain boundary. As the conductivity linearly increases with increasing grain size, the larger grain size in LTO-2 than LTO-1 could be the source of lower charge transfer resistance as shown by EIS studies in this work(58). CVs of LTO electrodes in AA solutions show the lowest overpotential required for electrooxidation of AA at the LTO-2 electrode. This result is expected as this electrode material is associated with the lowest charge transfer resistance witnessed by EIS studies. The LTO-2 electrode possesses the highest value of double layer capacitance (36 µF/cm2) along with higher ECSA among all other electrode materials. Higher double layer capacitance in LTO-2 is due to the higher affinity of the LTO-2 surface than other electrodes toward adsorbing charged species including deprotonated ascorbic acid (AA). XPS analysis of various LTO samples illustrates different contributions of $Ta^{5+}$, $Ta^{4+}$, and $Ta^{3+}$ at the surface of these oxides. Even though all LTO samples show the presence of multivalent tantalum species on their surfaces, they all differ in contribution of Ta oxidation states. LTO-2 comprises the highest amount of $Ta^{5+}$ on its surface. The high-resolution Li 1s spectrum of LTO-2 suggests that this sample possesses a more desirable structure in comparison to other synthesized samples due to allowing insertion of more Li atoms at the interstitial sites rather than the substitutional sites. Higher insertion of Li atoms at the interstitial sites in LTO-2 leads to a smaller change in coordination number and oxidation states of Ta atoms. The O 1s deconvoluted peak of LTO-2 illustrates the lower percentage of oxygen vacancies at the surface than other LTO samples which is in agreement with the domination of $Ta^{5+}$ in this material. Q-pole SIMS analysis has shed more light on the lithium atom distribution within LTO samples and provide more evidence on how that would lead to different electrochemical behaviors. According to this analysis, lithium atoms predominantly exist at the surface of LTO-0.5, LTO-1, and LTO-3 rather than in deeper levels of these materials. However, Q-pole SIMS analysis of LTO-2 shows a different situation where the lithium atom presence is more pronounced at the bulk of the material than its surface. The result of Q-pole SIMS analysis on LTO samples determines the higher diffusion of the lithium atoms in LTO-2 than other LTO materials. The lithium diffusion behavior in LTO samples could also explain tantalum valence states and oxygen vacancies on the surface of these species. XPS and Q-pole SIMS analyses show that oxygen vacancies and lower-valent tantalum are prevalent in LTO samples where the occurrence of lithium atoms is significant. Lithium incorporation is accompanied by oxygen vacancy formation that is preceded by $Ta^{5+}$

reduction to lower valence states. Higher abundance of lithium atoms at deeper depths of LTO-2 than its surface denotes the better diffusion of these atoms in LTO-2 than other samples. Lower overpotential required for AA oxidation and lower charge transfer resistance of LTO-2 can be explained by its higher oxygen vacancy concentration in the bulk where the lithium atoms are dominant. Mott-Schottky analysis enables finding the charge carrier density and flat band potential of LTO species. Electrochemical behavior of LTO electrode materials is related to how lithium atoms can be accommodated in these oxides. Mott-Schottky plots suggest that LTO species are all n-type semiconductors that means the non-stoichiometric amount of lithium atoms enter LTO lattices and they are localized at their interstitial sites.[59] LTO-2 is associated with the lowest carrier (electrons for n-type semiconductors) concentration and flat band potential values among all other species. The better performance of LTO-2 in electrooxidation of AA can now be justified by its lower carrier concentration, since in an electrooxidation reaction an electron is supposed to be transferred from the highest occupied molecular orbital (HOMO) of the analyte to the lowest unoccupied molecular orbital (LUMO) of the electrode. Lithium incorporation results in the addition of new energy levels to the oxides. Possessing low carrier concentration that is equivalent to less crowded molecular orbital energy levels, LTO-2 can facilitate the electron transfer from the AA HOMO to its LUMO. This facile electron transfer is due to the lower electrostatic repulsion between the isolated electrons from AA and charge carriers in LTO-2. Moreover, LTO-2 represents the lowest value of flat band potential in comparison to other lithium incorporated samples. Low flat band potential in LTO-2 is an indication of the relatively higher activity of this material in charge transfer across electrode/electrolyte interfaces than the other materials studied in this work. The lower flat band potential of LTO-2 with respect to other LTO-2 samples is in a good agreement with the low equilibrium potential between the LTO-2 electrode and AA solution obtained by the potentiodynamic analysis. These two tests can collectively reaffirm that the adsorption of deprotonated ascorbic acid (AA⁻) is more thermodynamically favored on LTO-2 rather than other materials which are studied in this work. The higher affinity of AA⁻ to LTO-2 is rooted in higher $Ta^{5+}$ concentration on the surface of this electrode. The adsorption of AA⁻ on the surface of LTO-2 is endorsed by the CV of the LTO-2 electrode submerged in AA solution and then transferred to the KCl solution. CV of the LTO-2 electrode in the KCl solution is characterized by a pair of redox peaks that are not observed when CV is run on the same electrode but in AA solution. The emergence of redox peaks in CV is attributed to the one electron transfer between the deprotonated ascorbic acid (AA⁻) and ascorbyl radical (AA·⁻). However, as shown in Fig. S7, the redox peaks for the LTO-2 electrode in KCl solution are separated by approximately 600 mV that is 10 times greater than the theoretical value for the potential difference of anodic and cathodic current in a reversible electron transfer. Complexation of ascorbic acid with transition metals has been reported by various research groups[60–62]. This complexation is characterized by monodentate and bidentate chelating of oxygen atoms bound to C2 and C3 carbons on AA structure to the hard metal ions. The binding of AA⁻ and AA·⁻,

respectively known as monodentate and bidentate ligands to the metal ions are associated with different coordination strengths. The cause of irreversibility of electron transfer of the surface reaction at the LTO-2 electrode is an indication of the various chelating strengths of AA⁻ and AA·⁻ to the $Ta^{5+}$ as the hard metal ion. That being said, the chemically reversible but electronically irreversible nature of LTO-2's CV implies that the analyte and its oxidized form are attached to the surface of the LTO-2 electrode and none of them are capable of leaving the electrode surface as its potential is altered (see in Fig. 7). Even though tweaking the electrode potential is not associated with a significant chemical structure alteration in the analyte, this leads to the oxidation of AA⁻ to AA·⁻ as it is proposed as the first step involved in the oxidation of ascorbic acid[63]. This monodentate-to-bidentate ligand transformation justifies that the irreversible electron transfer process as AA·⁻ can more firmly attach to $Ta^{5+}$, and requires more electrical energy to be oxidized back to AA⁻. On the contrary, CV of the LTO-2 electrode in AA solution is not featured with a redox pair and only shows an irreversible wave which is characteristic of a chemically irreversible reaction. The oxidation wave observed in this CV is characterized by lower overpotential and higher current density in compare to the oxidation peak in the surface reaction. The absence of the redox pair states that the chelation of AA⁻ and AA·⁻ is no longer either happening or significant. Therefore, the observed peak in CV can be attributed to the oxidation reaction of mono-protonated ascorbic acid that diffuses to the working electrode surface. As revealed by the Q-pole SIMS analysis, at the deeper depths of the LTO-2 sample the lithium content increases, and this may induce reduction of $Ta^{5+}$ to $Ta^{4+}$ and $Ta^{3+}$ species. This reduction is associated with a spontaneous oxygen vacancy inclusion triggered by a charge compensation mechanism. This oxygen vacancy formation is given by Kröger-Vink notation for a lithium dopant on a $Ta^{5+}$ site:
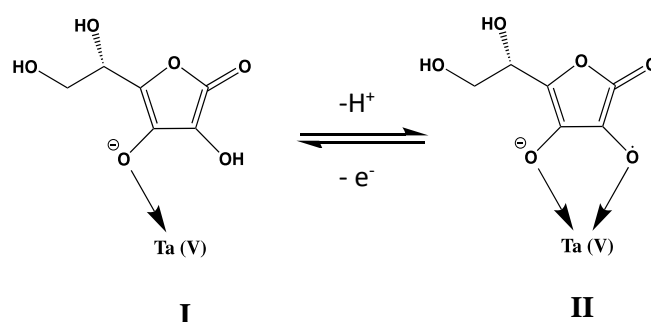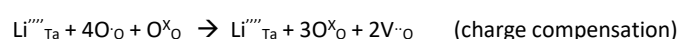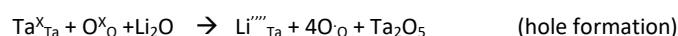


**Fig. 7** Oxidation of tantalum (V) - chelated (I) monodentate (mono) protonated ascorbic acid to (II) ascorbate radical.

$$Ta^{X}_{Ta} + O^{X}_{O} + Li_2O \rightarrow Li''''_{Ta} + 4O·_{O} + Ta_2O_5 \qquad \text{(hole formation)}$$

$$Li''''_{Ta} + 4O·_{O} + O^{X}_{O} \rightarrow Li''''_{Ta} + 3O^{X}_{O} + 2V··_{O} \qquad \text{(charge compensation)}$$

where $Ta^{X}_{Ta}$ and $O^{X}_{O}$ are neutral tantalum cation and oxygen anion respectively on $Ta^{5+}$ and $O^{2-}$ lattice sites, $Li''''_{Ta}$ is the lithium

substituting a $Ta^{5+}$ site, $O^{\cdot}_O$ is the hole, and $V^{\cdot\cdot}_O$ is the formed oxygen vacancy. The lower overpotential of in the chemically irreversible CV can be attributed to the higher conductivity at the bulk of the LTO-2 electrode due to the introduction of oxygen vacancy. The irreversible nature of the CV also represents the rare possibility of $AA^-$ chelation at the bulk of LTO-2 where less $Ta^{5+}$ should technically be present due to the presence of higher lithium content than its surface. Consequently, only a one step, two-electron, two-proton oxidation of the electro-active $AA^-$ to electro-inactive dehydroascorbic acid (DHAA) is feasible(63).

## Conclusions

Porous Lithium-incorporated tantalum oxides were synthesized successfully by using a reverse micelle templating method. Lithium incorporation and diffusion behavior in tantalum-based oxides define the electrochemical properties of these oxide systems. LTO-2 possesses the best electrocatalytic behavior among all other synthesized samples in this work. LTO-2 is more permeable to lithium than other LTO samples. Lithium permeability of the LTO-2 sample leads to oxygen vacancy formation in the bulk of the sample that facilitates the electron transfer between the analyte and the LTO-2 electrode's subsurface. The electrooxidation of AA at LTO-2 occurs through both diffusion-controlled and adsorption-controlled processes due to the gradient distribution of lithium atoms in this sample. Having high lithium permeability and moderate conductivity, $Li_{5.04}Ta_{6.16}O_{17.92}$ can be further studied as electrode materials in other electrochemical devices such as Li-ion batteries in future work.

## Conflicts of interest

There are no conflicts to declare.

## Acknowledgements

## References

1. Chaneliere C, Autran JL, Devine RAB, Balland B. Tantalum pentoxide (Ta2O5) thin films for advanced dielectric applications. Mater Sci Eng R Reports. 1998;22(6):269–322.
2. Zhao Y, Li C, Zhao W, Du Q, Chi B, Sun J, et al. Electrocatalytic oxidation of ascorbic acid on a lithium-doped tantalum oxide film coated electrode. Electrochim Acta . 2013;107:52–8.
3. Chang JP, Steigerwald ML, Fleming RM, Opila RL, Alers GB. Thermal stability of Ta2O5 in metal-oxide-metal capacitor structures. Appl Phys Lett. 1999;74(24):3705–7.
4. Yun S, Wang L, Guo W, Ma T. Non-Pt counter electrode catalysts using tantalum oxide for low-cost dye-sensitized solar cells. Electrochem commun. 2012;24(1):69–73.
5. Ishihara A, Tamura M, Matsuzawa K, Mitsushima S, Ota KI. Tantalum oxide-based compounds as new non-noble cathodes for polymer electrolyte fuel cell. Electrochim Acta. 2010;55(26):7581–9.
6. Ohgi Y, Ishihara A, Matsuzawa K, Mitsushima S, Ota KI, Matsumoto M, et al. Oxygen reduction reaction on tantalum oxide-based catalysts prepared from TaC and TaN. Electrochim Acta. 2012;68:192–7.
7. Sata S, Awad MI, El-Deab MS, Okajima T, Ohsaka T. Hydrogen spillover phenomenon: Enhanced reversible hydrogen adsorption/desorption at Ta 2 O 5 -coated Pt electrode in acidic media. Electrochim Acta. 2010;55(10):3528–36.
8. Zhao Y, Wang R, Han Z, Li C, Wang Y, Chi B, et al. Electrooxidation of methanol and ethanol in acidic medium using a platinum electrode modified with lanthanum-doped tantalum oxide film. Electrochim Acta. 2015;151:544–51.
9. Ishihara A, Tamura M, Ohgi Y, Matsumoto M, Matsuzawa K, Mitsushima S, et al. Emergence of oxygen reduction activity in partially oxidized tantalum carbonitrides: Roles of deposited carbon for oxygen-reduction-reaction-site creation and surface electron conduction. J Phys Chem C. 2013;117(37):18837–44.
10. Yang X, Mo Q, Guo Y, Chen N, Gao Q. Reduced-graphene-oxide supported tantalum-based electrocatalysts: Controlled nitrogen doping and oxygen reduction reaction. Appl Surf Sci. 2018;434:243–50.
11. Kong F, Tao S, Qian B, Gao L. Facile synthesis of MTaO 4 (M = Al, Cr and Fe) metal oxides and their application as anodes for lithium-ion batteries. Ceram Int. 2018;44(8):8827–31.
12. Manukumar KN, Kishore B, Manjunath K, Nagaraju G. Mesoporous Ta2O5 nanoparticles as an anode material for lithium ion battery and an efficient photocatalyst for hydrogen evolution. Int J Hydrogen Energy. 2018;43(39):18125–35.
13. Awaludin Z, Okajima T, Ohsaka T. Preparation of reduced tantalum pentoxide by electrochemical technique for oxygen reduction reaction. J Power Sources. 2014;268:728–32.
14. Awaludin Z, Safuan M, Okajima T, Ohsaka T. Investigating the physical and electrochemical effects of cathodic polarization treatment on TaO<inf>x</inf>. J Mater Chem A. 2015;3(32):16791–800.
15. Xiao W, Huang X, Song W, Yang Y, Herng TS, Xue JM, et al. High catalytic activity of oxygen-induced (200) surface of Ta2O5 nanolayer towards durable oxygen evolution reaction. Nano Energy. 2016;25:60–7.
16. Xia S, Ni J, Savilov S V., Li L. Oxygen-deficient Ta2O5 nanoporous films as self-supported electrodes for lithium microbatteries. Nano Energy.

2018;45(January):407–12.

17. Almeida Alves CF, Calderón S V., Dias D, Carvalho S. Influence of Oxygen content on the electrochemical behavior of Ta1-xOx coatings. Electrochim Acta. 2016;211:385–94.

18. Gritsenko VA, Perevalov T V., Voronkovskii VA, Gismatulin AA, Kruchinin VN, Aliev VS, et al. Charge Transport and the Nature of Traps in Oxygen Deficient Tantalum Oxide. ACS Appl Mater Interfaces. 2018;10(4):3769–75.

19. Xue L, He H, Liu C, Zhang C, Zhang B. Promotion effects and mechanism of alkali metals and alkaline earth metals on cobalt-cerium composite oxide catalysts for N2O decomposition. Environ Sci Technol. 2009;43(3):890–5.

20. Lawrence SA, Stevenson S, Mavadia K, Sermon PA. Solid-State Properties of Some Polycrystalline Alkali-Metal Tungsten Bronzes. Proc R Soc A Math Phys Eng Sci. 2006;411(1840):95–121.

21. Lindsay R, Michelangeli E, Daniels BG, Polcik M, Verdini A, Floreano L, et al. Surface to bulk charge transfer at an alkali metal/metal oxide interface. Surf Sci. 2003;547(1–2):14–9.

22. Vettraino M, Trudeau M, Antonelli DM. Synthesis and characterization of a new family of electroactive alkali metal doped mesoporous Nb, Ta, and Ti oxides and evidence for an Anderson transition in reduced mesoporous titanium oxide. Inorg Chem. 2001;40(9):2088–95.

23. Allen RN, Shukla MK, Burda J V, Leszczynski J. Cations. 2006;6139–44.

24. Greshnyakov ED, Lisjikh BI, Pryakhina VI, Nebogatikov MS, Shur VY. Charged domain walls in lithium tantalate with compositional gradients produced by partial VTE process. IOP Conf Ser Mater Sci Eng. 2019;699(1).

25. Pryakhina VI, Greshnyakov ED, Lisjikh BI, Akhmatkhanov AR, Alikin DO, Shur VY, et al. As-grown domain structure in lithium tantalate with spatially nonuniform composition. Ferroelectrics. 2018;525(1):47–53.

26. Fujii S, Uda S, Maeda K, Nozawa J, Koizumi H, Fujiwara K, et al. Growth of congruent-melting lithium tantalate crystal with stoichiometric structure by MgO doping. J Cryst Growth. 2013;383:63–6.

27. Hollerweger R, Holec D, Paulitsch J, Bartosik M, Daniel R, Rachbauer R, et al. Complementary ab initio and X-ray nanodiffraction studies of Ta2O5. Acta Mater. 2015;83:276–84.

28. Santoro A, Roth RS, Austin M. Powder neutron diffraction study of the nonstoichiometric solid solution of lithium tantalate 9LiTaO 3 :Ta 2 O 5 . Acta Crystallogr Sect B Struct Crystallogr Cryst Chem. 1982;38(4):1094–8.

29. Blasse G. On the Structure of some Compounds Li3Me5+O4, and some other Mixed Metal Oxides Containing Lithium. ZAAC - J Inorg Gen Chem. 1964;331(1–2):44–50.

30. Sing KSW, Williams RT. Physisorption hysteresis loops and the characterization of nanoporous materials. Adsorpt Sci Technol. 2004;22(10):773–82.

31. Leal-Egaña A, Dietrich-Braumann U, Díaz-Cuenca A, Nowicki M, Bader A. Determination of pore size distribution at the cell-hydrogel interface. J Nanobiotechnology. 2011;9:1–7.

32. Sing K. The use of nitrogen adsorption for the characterisation of porous materials. Colloids Surfaces A Physicochem Eng Asp. 2001;187–188:3–9.

33. Buabthong P, Stasiewicz NB, Mitrovic S, Lewis NS, Buabthong P, Stasiewicz NB, et al. Vanadium , niobium and tantalum by XPS. 2017;024001.

34. Simpson R, White RG, Watts JF, Baker MA. XPS investigation of monatomic and cluster argon ion sputtering of tantalum pentoxide. Appl Surf Sci. 2017;405:79–87.

35. Gonçalves R V., Wojcieszak R, Uberman PM, Teixeira SR, Rossi LM. Insights into the active surface species formed on Ta2O 5 nanotubes in the catalytic oxidation of CO. Phys Chem Chem Phys. 2014;16(12):5755–62.

36. Awaludin Z, Safuan M, Okajima T, Ohsaka T. Investigating the physical and electrochemical effects of cathodic polarization treatment on TaOx. J Mater Chem A. 2015;3(32):16791–800.

37. Subba Reddy C V., Jin AP, Han X, Zhu QY, Mai LQ, Chen W. Preparation and characterization of (PVP + V2O5) cathode for battery applications. Electrochem commun. 2006;8(2):279–83.

38. Lu JG, Zhang YZ, Ye ZZ, Zeng YJ, He HP, Zhu LP, et al. Control of p- and n-type conductivities in Li-doped ZnO thin films. Appl Phys Lett. 2006;89(11):1–4.

39. Zhang L, Liu F, Brinkman K, Reifsnider KL, Virkar A V. A study of gadolinia-doped ceria electrolyte by electrochemical impedance spectroscopy. J Power Sources. 2014;247:947–60.

40. Dutta B, Wu Y, Chen J, Wang J, He J, Sharafeldin M, et al. Partial Surface Selenization of Cobalt Sulfide Microspheres for Enhancing the Hydrogen Evolution Reaction. ACS Catal. 2019;9(1):456–65.

41. Faber MS, Dziedzic R, Lukowski MA, Kaiser NS, Ding Q, Jin S. High-performance electrocatalysis using metallic cobalt pyrite (CoS 2) micro- and nanostructures. J Am Chem Soc. 2014;136(28):10053–61.

42. Biesheuvel PM, Dykstra JE. The difference between Faradaic and Nonfaradaic processes in Electrochemistry. 2018;1–10.

43. Albery WJ, O'Shea GJ, Smith AL. Interpretation and use of Mott-Schottky plots at the semiconductor/electrolyte interface. J Chem Soc - Faraday Trans. 1996;92(20):4083–5.

44. Bera B, Chakraborty A, Kar T, Leuaa P, Neergat M. Density of States, Carrier Concentration, and Flat Band Potential Derived from Electrochemical Impedance Measurements of N-Doped Carbon and Their Influence on Electrocatalysis of Oxygen Reduction Reaction. J Phys Chem C. 2017;121(38):20850–6.

45. Deshpande A, Kelkar S, Rayalu S, Ogale S. Orthorhombic/cubic Cd2SnO4 nanojunctions: Enhancing solar water splitting efficiency by the suppression of charge recombination. J Mater Chem A. 2014;2(2):492–9.

46. Haerifar M, Azizian S. Mixed surface reaction and diffusion-controlled kinetic model for adsorption at the

solid/solution interface. J Phys Chem C. 2013;117(16):8310–7.

47. Hu IF, Kuwana T. Oxidative Mechanism of Ascorbic Acid at Glassy Carbon Electrodes. Anal Chem. 1986;58(14):3235–9.

48. Xue L, He H, Liu C, Zhang C, Zhang B. Promotion effects and mechanism of alkali metals and alkaline earth metals on cobalt-cerium composite oxide catalysts for N2O decomposition. Environ Sci Technol. 2009;43(3):890–5.

49. Grewe T, Tuÿsüz H. Alkali metals incorporated ordered mesoporous tantalum oxide with enhanced photocatalytic activity for water splitting. J Mater Chem A. 2016;4(8):3007–17.

50. Carey JJ, Nolan M. Enhancing the oxygen vacancy formation and migration in bulk chromium(III) oxide by alkali metal doping: A change from isotropic to anisotropic oxygen diffusion. J Mater Chem A. 2017;5(30):15613–30.

51. Lawrence SA, Stevenson S, Mavadia K, Sermon PA. Solid-State Properties of Some Polycrystalline Alkali-Metal Tungsten Bronzes. Proc R Soc London, Ser A Math Phys Sci. 1987;411(1840):95–121.

52. Dutta B, Clarke R, Raman S, Shaffer TD, Achola L, Nandi P, et al. Lithium promoted mesoporous manganese oxide catalyzed oxidation of allyl ethers. Nat Commun. 2019;10(1):1–6.

53. Nolan M. Enhanced oxygen vacancy formation in ceria (111) and (110) surfaces doped with divalent cations. J Mater Chem. 2011;21(25):9160–8.

54. Nolan M. Charge compensation and Ce3+ formation in trivalent doping of the CeO2(110) surface: The key role of dopant ionic radius. J Phys Chem C. 2011;115(14):6671–81.

55. Sweeney KL, Halliburton LE. Oxygen vacancies in lithium niobate. Appl Phys Lett. 1983;43(4):336–8.

56. S E L F - T R A P P E D E L E C T R O N S IN L I T H I U M TANTALATE " K.L. SWEENEY t and L.E. H A L L I B U R T O N. 1986;116(2):81–4.

57. Yan T, Zheng F, Yu Y, Qin S, Liu H, Wang J, et al. Formation mechanism of black LiTaO3 single crystals through chemical reduction. J Appl Crystallogr. 2011;44(1):158–62.

58. Tan A, Chu Kun Kuo, Nicholson PS. The influence of grain-boundaries on the conductivity and ion-exchange rate of β″ -alumina polycrystalline isomorphs. Solid State Ionics. 1991;45(1–2):137–42.

59. Fang Z, He H, Gan L, Li J, Ye Z. Understanding the Role of Lithium Doping in Reducing Nonradiative Loss in Lead Halide Perovskites. Adv Sci. 2018;5(12):1–6.

60. Cesario D, Furia E, Mazzone G, Beneduci A, De Luca G, Sicilia E. Complexation of Al3+ and Ni2+ by l -Ascorbic Acid: An Experimental and Theoretical Investigation. J Phys Chem A. 2017;121(51):9773–81.

61. Buettner KM, Collins JM, Valentine AM. Titanium(IV) and vitamin C: Aqueous complexes of a bioactive form of Ti(IV). Inorg Chem. 2012;51(20):11030–9.

62. Zümreoglu-Karan B. The coordination chemistry of Vitamin C: An overview. Coord Chem Rev. 2006;250(17–18):2295–307.

63. Tu YJ, Njus D, Schlegel HB. A theoretical study of ascorbic acid oxidation and HOO / O 2- Radical scavenging. Org

Biomol Chem. 2017;15(20):4417–31.

# Graphical Abstract
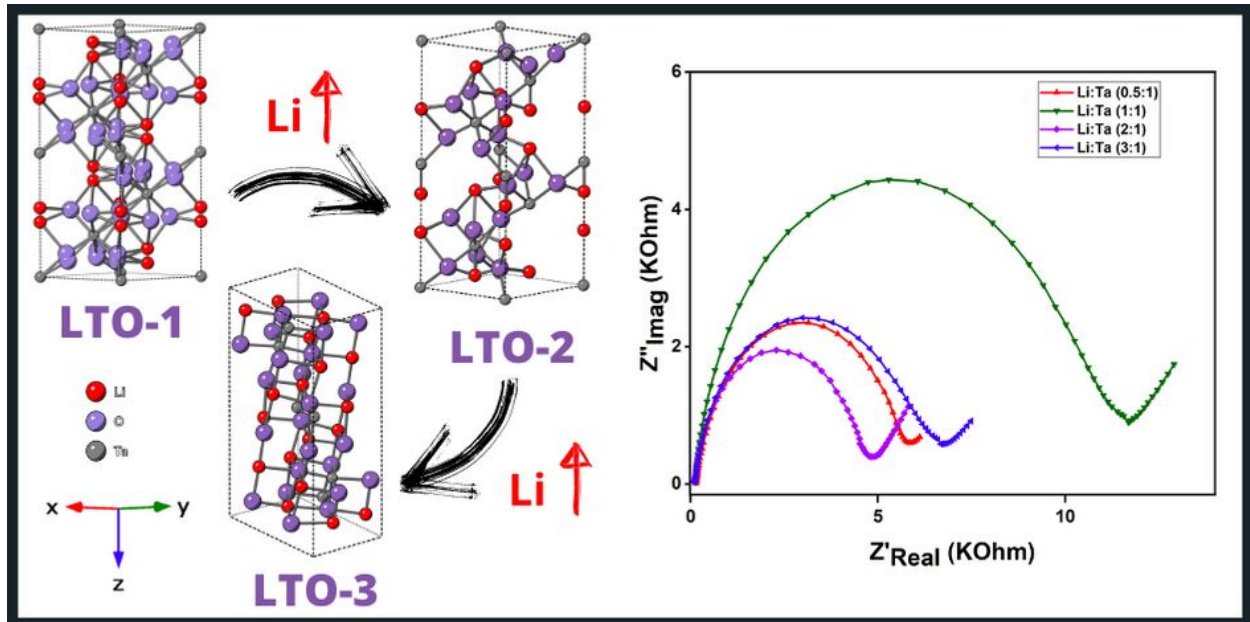


Phase evolution of lithium incorporated tantalum oxides, triggered by Li addition, leads to the change in electrical properties of oxides.